Mechanics of Materials 177 (2023) 104532

Contents lists available at ScienceDirect

Mechanics of Materials

journal homepage: www.elsevier.com/locate/mecmat

Research paper

Coupling between mechanical stresses and lithium penetration in a lithium ion battery

Amine Saidi [a,b], Anne Tanguy [a,*], Marion Fourmeau [a], Gergely Molnár [a], Abderraouf Boucherif [b], Denis Machon [b,c]

[a] Univ. Lyon, INSA-Lyon, CNRS UMR5259, LaMCoS, F-69621, France
[b] Laboratoire Nanotechnologies Nanosystèmes (LN2) - CNRS IRL-3463, Institut Interdisciplinaire d'Innovation Technologique (3IT), Université de Sherbrooke, 3000 Boulevard de l'Université, Sherbrooke, J1K OA5 Québec, Canada
[c] Univ. Lyon, Université Claude Bernard Lyon 1, CNRS, Institut Lumière Matière, F-69622, Lyon, France

ARTICLE INFO

Keywords:
Mechanical properties
Anode
Lithiation
Molecular dynamics
Crystalline silicon
Amorphous silicon

ABSTRACT

Silicon-based anodes are an attractive choice for the future of energy storage. However, mechanical stresses generated during lithiation induce a rapid degradation of the anodes. The coupling between mechanical and (electro)chemical phenomena during lithiation is investigated using Molecular Dynamics simulations. First, the diffusion regime of lithium atoms in the silicon is found to depend drastically on the crystalline orientations and on the applied pressure. Above a threshold pressure, a ballistic motion of lithium along certain crystallographic planes is observed. Second, the local complex stress field generated by the lithiation has been computed using a coarse-graining method including thermal effects. It appears to be strongly dependent on the density of lithium in the lithiated layer, on the temperature, and on the crystalline orientation of the free surface. The resulting very high values of the locally induced pressures can be related to the progressive amorphization of the silicon support.

1. Introduction

The increased need for efficient energy storage for small and medium-sized applications, such as mobile electronic devices and electric vehicles, has been well identified by various international reports as an essential element in the transition to renewable energy sources (Armand et al., 2020). One of the proposed solutions is Lithium Ion Battery (LIB), easy-to-use, partly recyclable and cost effective. However, the current technology based on graphite electrodes has reached its optimum. An alternative is the use of silicon-based anodes in LIB, because silicon has a theoretical capacity of 3579 mAh g^{-1}. This is 10 times higher than the traditional graphite electrode (Obrovac and Chevrier, 2014). Silicon is also advantageous in terms of price, abundance and non-toxicity. However, it presents an important volume expansion during lithiation (>300 %) (Obrovac and Christensen, 2004), associated with an extreme brittleness at ambient temperature. This leads to a rapid decrease of the lithium loading capacity due to various failure modes during the first charge and discharge cycles (Wu and Cui, 2012; Zhang et al., 2020). Therefore, it clearly appears that understanding mechanical behaviour of silicon during lithiation is at the core of a technology breakthrough (McDowell et al., 2016; Zhao and Cui, 2016; Zhang et al., 2020). As a LIB is a complex system with multi-physical and chemical mechanisms at work, the interactions and couplings between these different phenomena must be better understood to better apprehend the functioning of a battery and to optimize it (Yang et al., 2015). This is particularly the case with silicon-based anode for which these effects cause chemo-mechanical degradations such as fracture or electrical contact loss during cycling. These links between electrochemical transformations and solid mechanics often play a decisive role in the behaviour and stability of alloy anodes.

During the life cycle of a battery system, the fabrication of the silicon anode leads to initial residual stresses in the anode even before the use of the battery. During its use (charge and discharge), the electric field generates diffusion forces on the lithium ions, and their penetration inside the silicon structure leads to a complex internal stress field (Zhang et al., 2020). In addition, temperature and external pressure influence this stress field and can then be considered as control parameters during the use of batteries to increase their lifetime. The effect of stresses on the performances of a anodes has been recently demonstrated (Berckmans et al., 2019). However, while mechanical constraints are crucial to pilot the durability of lithium ions batteries, mainly macroscopic studies of the mechanical properties of these systems have been performed up to now (Kumta et al., 2021; Huang

* Corresponding author.
E-mail address: anne.tanguy@insa-lyon.fr (A. Tanguy).

https://doi.org/10.1016/j.mechmat.2022.104532
Received 20 September 2022; Received in revised form 9 November 2022; Accepted 17 November 2022
Available online 22 November 2022

and Guo, 2021; Shang et al., 2021; Bagheri et al., 2019). Mesoscopic models have been proposed recently for the constitutive laws of silicon in the presence of lithium (Bagheri et al., 2021; Lu and Ni, 2015), but they need as well a proper description of the mechanical properties at the atomic scale to get a realistic value the parameters involved. In the last decades, new coarse-graining methods have been developed to access the mechanical properties down to the atomic scale (Goldhirsch and Goldenberg, 2002, 2005), preserving the mass and momentum conservation equations at all scales. These methods have been successfully used in molecular dynamics simulations of crystalline as well as amorphous materials (Tsamados et al., 2009; Molnár et al., 2016), including materials with free surfaces (Zimmerman et al., 2004). They allow getting an accurate description of the local mechanical quantities like local strain and stress components that could be responsible for materials damage.

In this article, we investigate two major effects. First, we study how the external hydrostatic pressure can have an effect on the penetration force and modify the lithium diffusion process. The range of pressure we investigated has never been evaluated before, and we report a regime change in the lithium diffusion above a pressure threshold. In addition, by comparing different crystalline orientations and amorphous configurations, we demonstrated the dependence of the regime change with the orientations. Second, we show, combining molecular dynamics simulations with local as well as global mechanical analysis, the evolution of the stress distribution and of the local structure in a crystalline silicon absorbing lithium ions. The nature of the stress field questions the driving force of the amorphization during lithiation. Depending if this transformation is chemically- or mechanically- driven, the control of this phenomenon that is detrimental for the LIB will vary.

The manuscript is organized as follows. Section 2 describes the silicon samples, with a calculation of local residual stresses and their temperature dependence, as well as global elastic moduli. In Section 3, the critical penetration force of a lithium atom in terms of environmental pressure is computed for three different orientations of the silicon crystal, and for different amorphous configurations. Finally, Section 4 discusses the impact of the lithiation process on the local silicon structure, as well as local deviatoric and spherical parts of Coarse-grained (CG) stress tensors.

2. Numerical model description and validation

We present here the different numerical tools used along this study.

2.1. Samples and molecular interactions

Molecular potential simulations are carried out using LAMMPS software (Large-scale Atomic/Molecular Massively Parallel Simulator) (Thompson et al., 2022). The interactions between Si–Si and Li–Si atoms are modelled with the second Nearest-Neighbour Modified Embedded AtoMethod (2NN MEAM) potential (Baskes, 1992). Accordingly, the total energy of the system has the form

$$E = \sum_i \left\{ F_i(\bar{\rho}_i) + \frac{1}{2} \sum_{i \neq j} \phi_{ij}(r_{ij}) \right\} \tag{1}$$

where i and j designate atoms, F_i is the embedding energy, ρ_i is the background electron density, ϕ_{ij} is the pair potential and r_{ij} is the interatomic spacing. The parameter values of the potential 2NN MEAM for Si and Li are taken from Baskes (1992) and those for the Li–Si interactions are from Wang et al. (2013) .

The crystalline structure studied in this work is a $12 \times 12 \times 12$ lattice with periodic boundary conditions in the three directions. Three different crystal orientations are investigated for the normal to the free surface ($\langle 100 \rangle$, $\langle 110 \rangle$ and $\langle 111 \rangle$). Additionally, three different amorphous systems are studied. For the amorphous configurations, the initial positions are obtained as in Fusco et al. (2010) from a silicon structure with a cell dimension of 180 Å × 180 Å × 180 Å equilibrated at 1700 K during 1 ns then cooled to 0K with a cooling rate of 20 K ps^{-1}. The three amorphous systems studied correspond to: 1) without annealing, 2) with additional thermal ramping to 300 K in 1 ps and then annealing at 300 K during 50 ps before final cooling down to 10^{-3} K during 50 ps, 3) with annealing at 2000 K using the same procedure. In this work, the numerical thermostat used is always a Nose–Hoover thermostat with a damping parameter of 10 fs (corresponding to 100 time steps).

It is worth noting that the Solid-Electrolyte Interphase (SEI) is not included in the systems studied here. The primary objective is to better understand the mechano-chemical couplings in the Li–Si system. In addition, the SEI is a complex, multi-phase and heterogeneous system that is difficult to model using Molecular Dynamics that requires a good knowledge of the composition, structure, spatial distribution, etc. The effect of SEI on mechanical properties can be better captured by using macroscopic methods such as Finite Elements (McBrayer et al., 2021).

2.2. Stress calculations

All stresses are calculated every 1 ps using the coarse graining (CG) formalism (Goldhirsch and Goldenberg, 2002, 2005) developed especially for atomistic simulations (Goldhirsch and Goldenberg, 2005, 2002). The coarse graining method is based on a spatial averaging allowing the preservation of the mass and of the momentum equations at any coarse-graining scale R. A Gaussian coarse-graining function ϕ (Tunuguntla et al., 2016) is used for all CG stress calculations

$$\phi(\mathbf{r}) = \frac{1}{(\sqrt{2\pi}R)^3} exp\left(\frac{-|\mathbf{r}|^2}{2R^2}\right) \tag{2}$$

at any position r with a standard deviation of $R = 5$ Å (coarse-graining length value R chosen to be consistent with the classical continuous mechanical modelling for crystalline as well as for amorphous silicon (Fusco et al., 2010)). This formalism allows connecting microscopic quantities defined at particle positions with a continuous field averaged over the vicinity of each particle.

The potential as well as the kinetic contributions to the stress components are taken into account in this calculation

$$\begin{cases} \sigma_{\alpha\beta}^{total}(\mathbf{r},t) = \sigma_{\alpha\beta}^{potential}(\mathbf{r},t) + \sigma_{\alpha\beta}^{kinetic}(\mathbf{r},t) \\ \sigma_{\alpha\beta}^{potential}(\mathbf{r},t) = -\sum \frac{1}{2} f_{ij\alpha}(t) r_{ij\beta}(t) \int_0^1 \phi(\mathbf{r} - \mathbf{r_i} + s\mathbf{r_{ij}}) ds \\ \sigma_{\alpha\beta}^{kinetic}(\mathbf{r},t) = -\sum m_i v_{i\alpha}(t) v_{i\beta}(t) \phi(\mathbf{r} - \mathbf{r_i}) \end{cases} \tag{3}$$

where α and β denote the spatial directions for components of vectors and matrices, $f_{ij\alpha}$ is the force particle j applies on particle i in the α direction ($f_{ij\alpha} = -\partial E / \partial r_{ij\alpha}$), $r_{ij\alpha}$ is the interatomic spacing between atoms i and j in the α direction, and $v_{i\alpha}$ is the velocity supported by atom i in α direction from coarse-grained velocity component at the same place (Goldhirsch and Goldenberg, 2005).

Two quantities of the stress tensor, the von Mises stress σ_{VM} and the hydrostatic stress σ_H, are defined by

$$\begin{cases} \sigma_{VM} = \sqrt{\frac{(\sigma_1 - \sigma_2)^2 + (\sigma_2 - \sigma_3)^2 + (\sigma_1 - \sigma_3)^2}{2}} \\ \sigma_H = -P = \frac{tr\left(\underline{\underline{\sigma}}\right)}{3} \end{cases} \tag{4}$$

where σ_i for $i = 1 \ldots 3$ are the principal stresses of any stress tensor. The von Mises stress quantifies the shear energy stored in the material, while the hydrostatic stress is a pressure (with opposite sign).

This methodology allows evaluating at each atom, the residual stress distributions in various silicon structures. The residual stresses, and the elastic moduli and their temperature-dependence for crystalline and amorphous silicon have been computed in Sections 2 and 3 respectively. The good agreement between the results of the simulations and the experimental data is a validation of the method and of the different parameters used.

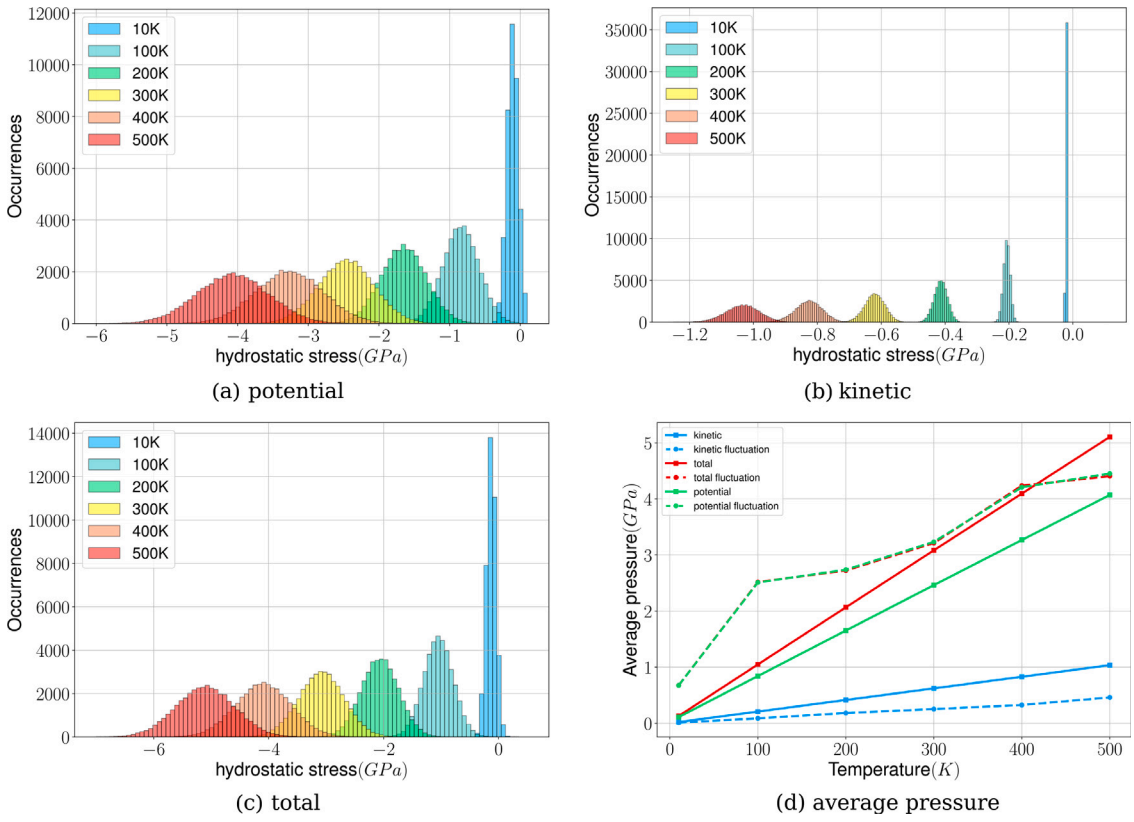

Fig. 1. Distribution of residual hydrostatic stress σ_H over the simulation box of ⟨100⟩ silicon structure with (a) potential, (b) kinetic and (c) total contributions, for different temperature values. (d) Average residual hydrostatic stress and its fluctuations versus temperature, with potential and kinetic contributions, for ⟨100⟩ silicon structure.

2.3. Residual stresses under various temperatures

We have equilibrated the three crystalline and three amorphous samples under an NVT ensemble (Number of atoms, Volume and Temperature are constant) at five different temperatures [10 K, 100 K, 200 K, 300 K, 400 K] during 120 ps. All stress tensor components are calculated by averaging stress values on each atom taken every 1 ps, over the last 100 ps of the equilibration phase to prevent statistical fluctuations induced by the thermostat.

Fig. 1 shows the distribution of the hydrostatic stress σ_H computed from kinetic, potential and total stress tensors, obtained for two different temperature values, for the ⟨100⟩ silicon crystal at rest. These stresses are called "residual stresses" since they correspond to the equilibrated stress state of the silicon crystal (quenched stresses).

Firstly, it appears that the kinetic residual stress amplitude is low compared to the potential residual stress amplitude at any temperature. Secondly, increasing the temperature leads to a linear increase in kinetic residual stress amplitude. The potential stress amplitude also increases with temperature since the volume of our simulation box is fixed. The width of the distributions also increases with temperature due to thermal agitation. This is clearly seen in Fig. 1(d) where the hydrostatic pressure and its fluctuations averaged over the simulation box, for each five temperature values (with potential, kinetic and total contributions) are given. The general trend is that the hydrostatic stress is compressive (positive pressure) and its intensity increases linearly when temperature increases. This is due to the thermal agitation of silicon atoms with a simulation box of *constant volume*.

2.4. Elastic moduli calculation

The variation of the global elastic moduli with respect to temperature can be evaluated by imposing strain components to the simulation boxes. This will enable to validate the numerical simulations through the mechanical properties obtained without any calibration of our model. Numerical simulations are divided into three steps. First, an initial structure is taken from the NVT equilibration (with residual stresses) at the target temperature. Then, strain loadings with strain steps $\epsilon_i = 10^{-4}$ in Voigt notation for $1 \leq i \leq 6$ (six loading cases xx, yy, zz, xy, xz, yz) are applied separately. Finally, each configuration is equilibrated under NVT ensemble during 120 ps. This procedure is repeated for the three crystalline orientation and for the amorphous configuration obtainned by the annealing at 300 K, and for each six temperature values (10 K, 100 K, 200 K, 300 K, 400 K, 500 K). A strain $\epsilon_i = 10^{-6}$ has also been used for one configuration, in order to check that the value chosen for the strain is sufficiently small to get results insensitive to the applied strain. For each loading case, the variations of potential, kinetic and total stress tensors are defined as the difference between final and residual stress values. The elastic moduli tensor is defined by the Hooke's relationship between stress and strain tensors with Voigt notation

$$\sigma_i^{total} = C_{ij}\epsilon_j \text{ where } i = 1 \dots 6 \tag{5}$$

To compute elastic moduli for a given silicon structure at a given temperature, six independent deformations have been imposed on the simulation box, and for each deformation the stress components have been computed. The system to solve then contains $6 \times 6 = 36$ linear equations allowing to determine the 21 anisotropic elastic moduli. This overdetermined linear system is solved using the least square method implemented in matlab software with QR algorithm (Kublanovskaya, 1962; Francis, 1962, 1961). Table 1 shows all the 21 elastic moduli components at each temperature obtained by error minimization, for the ⟨100⟩ crystalline silicon structure. Fig. 2 shows the evolution of 3 out of 21 moduli with respect to temperature. The values at room temperature (300 K) are of the same order as found in the literature (McDowell et al., 2013), with a deviation from the experimental values of less than 10%. For other crystalline orientations, ⟨110⟩ and

Table 1
Elastic moduli obtained by minimization error for the < 100 > silicon structure and an amorphous structure, at various temperature values.

	Calculated values (GPa)					Literature values (GPa)(Hall, 1967)
	10 K	100 K	200 K	300 K	400 K	298 K
C_{11}	163.62	163.29	162.92	162.59	162.15	$165.6 \pm 0.02\%$
C_{12}	65.01	65.16	65.34	65.41	65.75	$63.9 \pm 0.02\%$
C_{44}	73.78	73.49	73.15	72.85	72.42	$79.5 \pm 0.02\%$
C_{ij} $4 \leq j \leq 6, 1 \leq i < j$	0.0 ± 0.2	0.0 ± 0.2	0.0 ± 0.2	0.0 ± 0.2	0.0 ± 0.2	–
$E_{amorphous}$	–	–	107 ± 18	–	–	$165.6 \pm 0.02\%$
$\nu_{amorphous}$	–	–	$0,317 \pm 0.030$ *(adim)*	–	–	0.347 (Fusco et al., 2010)
with $C_{11} \approx C_{22} \approx C_{33}$, $C_{12} \approx C_{13} \approx C_{23}$ and $C_{44} \approx C_{55} \approx C_{66}$						

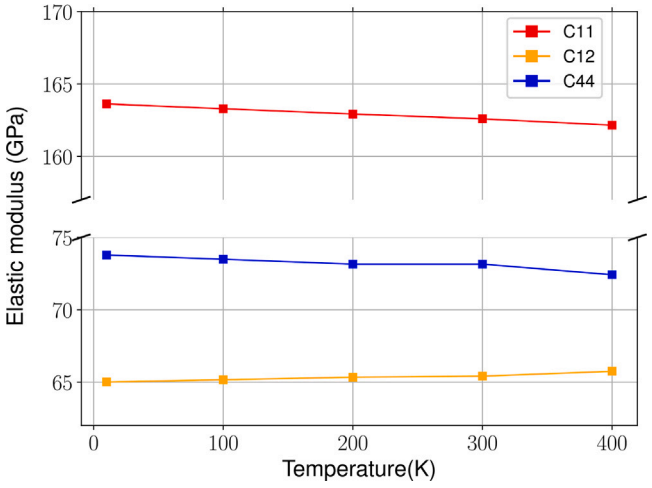

Fig. 2. C_{11}, C_{12} and C_{44} elastic moduli versus temperature, for ⟨100⟩ silicon structure.

⟨111⟩, the values obtained for C_{ij} are identical as soon as expressed in the same coordinate system with respect to the crystal. The amorphous silicon configuration at 300 K is shown to be nearly isotropic with a Young modulus $E = 107 \pm 18$ GPa and Poisson's ratio $\nu = 0.317 \pm 0.030$ (Fusco et al., 2010). To get these values, the best fit of the general compliance matrix to the isotropic matrix has been computed (see Appendix). The temperature influence on the moduli can be approximated to a linear function, with a decreasing slope of 3.7(1) MPa K^{-1} and 3.4(1) MPa K^{-1} for C_{11} and C_{44}, respectively. The experimental measurements of the C_{ij} in this temperature range show a non-linear behaviour (McSkimin, 1953). In the low-temperature regime, the results are similar (C_{11} varies by 3.1 MPa K^{-1}). However, at higher temperature, the temperature dependence of the C_{ij} increases. This behaviour probably originates from the fact that our simulations are at constant volume and that the silicon shows anomalous thermal expansion below 300 K (Middelmann et al., 2015).

The simulated mechanical properties of crystalline and amorphous silicon samples are in good agreement with the experimental data, showing the robustness of the methodology.

3. Critical lithium penetration force for different pressures and temperatures

In this section, the critical force necessary for a lithium ion to diffuse in the silicon structure as a function of pressure applied to silicon is computed. In the situation of a LIB, this force corresponds to an electrostatic force resulting from the effect of an applied electric field on Li ions.

3.1. Methodology

As illustrated in Fig. 3, simulation boxes are set for both crystalline and amorphous silicon structures to reproduce the insertion of a lithium atom in the silicon structure (lithiation process). The crystalline structures are constructed from a $8 \times 8 \times 18$ lattice of crystalline silicon for three different crystal orientations: ⟨100⟩, ⟨110⟩ and ⟨111⟩ (see Fig. 3(a) for the crystalline orientation ⟨100⟩). Additionally, an amorphous structure with annealing at 2000 K is used, that is illustrated in Fig. 3(b).

Firstly, for each crystalline orientation, the periodic silicon box without any lithium atom is subjected to a hydrostatic pressure. Periodicity conditions are imposed in the three directions. For each value of external pressure (from 0 to 20 GPa), the energy of the system is minimized by adjusting the positions of each atom. The size of the simulation box is updated at each iteration to obtain the targeted value of pressure. Next, an equilibration stage is performed at 300 K. The pressure and the temperature are regulated by a Nosé-Hoover barostat and thermostat with a damping parameter of 0.1 fs and 10 fs, respectively. After equilibrating silicon structures, the periodicity condition in the z-direction is removed and the size of the simulation box along z is increased by a factor of two, to get an empty space between the silicon sample and the limits of the box, and a free boundary condition on the samples surface. In the z-direction, the Nosé-Hoover barostat is replaced by an equivalent force applied on both the inferior and superior layers of atoms (red and yellow atomic layers, respectively, in Fig. 3). This procedure is necessary to prevent pressure variations and insure the stability of the free surface of silicon when a lithium atom is included in the simulation. The new structure is equilibrated for a period of 5 ps.

After this step of equilibration, a lithium atom is inserted in the middle of the vacuum above the silicon structure and subjected to a downward force field. The critical force is defined as the minimal value of the force, allowing a lithium atom to go continuously through the silicon structure. The critical force is estimated by iteration within the interval of [0.3, 5.0] eV $Å^{-1}$ using the bisection method. Under a given force, if the lithium atom goes through the silicon structure without getting trapped, the force applied is above the critical force. Otherwise, if the lithium atom is trapped in the silicon structure before 50 ps, the force applied is considered as lower than the critical force. The iterations are stopped when the interval reaches 0.001 eV $Å^{-1}$. The influence of the initial lithium atom position was also investigated by simulating at least 50 different positions in the x–y plane, for each crystalline structure orientation. However, the force variations were observed to be negligible so the initial Li atom position will not be accounted for in the rest of the study.

3.2. Critical force analysis

The critical forces for various silicon structures and various pressures, at $T = 300$ K, are illustrated in Fig. 4. Calculations of critical

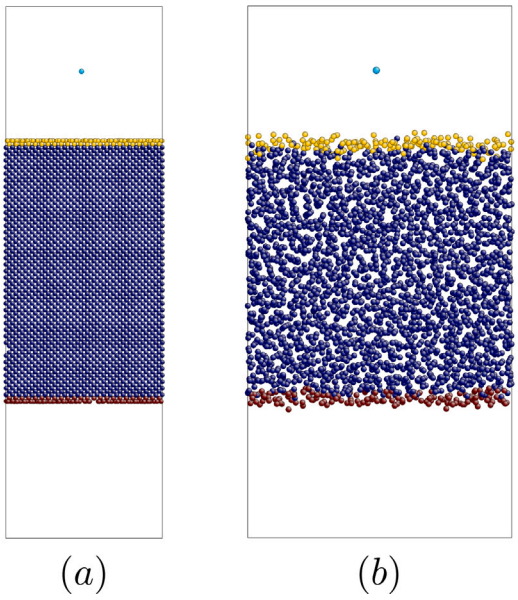

Fig. 3. Front view of simulation boxes for (a) ⟨100⟩ crystal orientation (b) amorphous silicon, with one lithium atom (skyblue atom). (For interpretation of the references to colour in this figure legend, the reader is referred to the web version of this article.)

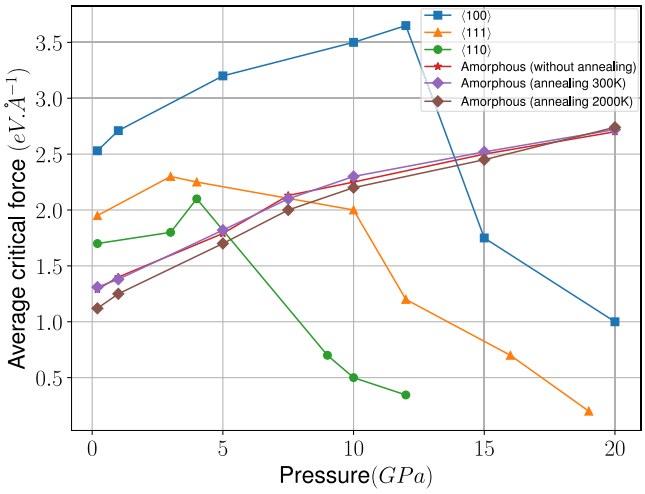

Fig. 4. Average critical penetration force versus pressure for various silicon structures at 300 K.

Table 2
Average critical penetration force for three silicon crystalline orientations, at two different pressure values, and comparison with literature values (Wang et al., 2013).

Crystal orientation	Literature values (Wang et al., 2013) (eV Å^{-1})	Calculated values (eV Å^{-1})	
		100 MPa	5 GPa
< 100 >	4.13	2.5	3.2
< 110 >	3.02	1.7	1.7
< 111 >	3.44	1.9	2.1

penetration forces have already been reported for crystalline silicon oriented in three crystal orientations ⟨100⟩, ⟨110⟩, and ⟨111⟩ for a temperature of 300 K (Table 2) (Wang et al., 2013). At low pressure (100 MPa), our results are comparable to the literature and show the same trend for the influence of crystal orientation, but with lower values. This can be explained by differences in numerical parameters (silicon structure, loading conditions, material model parameters) and, above all, by the criterion defining the critical force. Indeed, the critical force in Wang et al. (2013) is defined by the minimum force allowing a continuous diffusion of the lithium atom without getting trapped. This criterion leads to larger values of critical forces than our criterion, because it does not consider diffusion when a lithium atom is momentarily trapped but eventually continues finally to travel across the structure (Yan et al., 2015). However, the relative value of the critical forces are in agreement with Wang et al. (2013) as the critical force in ⟨100⟩ and ⟨111⟩ orientation is about 47% and 12% larger than in ⟨110⟩ case. The critical force values vary with the crystal orientation, while amorphous silicon with different configurations have very similar critical force values. It has been suggested that this tendency is related to the different angles between the direction of the diffusion barrier and the crystal orientation, i.e., the diffusion pathway is more direct in the case of ⟨110⟩ orientation (Wang et al., 2013).

For all silicon structures under pressure, the general trend in the low-pressure regime is an increase in the critical penetration force with increasing pressure. The lattice is compressed and induced a limitation of lithium atom diffusion. This observation is in agreement with previous studies on the effect of stresses on the diffusion coefficient. For instance, it has been shown experimentally that it decreases with compressive stresses for both crystalline and amorphous structures (Yang et al., 2015; Pan et al., 2015; McDowell et al., 2012; McBrayer et al., 2021). For the amorphous configurations, the monotonic increase may be related to the variation of the activation volume (Pan et al., 2015).

For higher pressure values and for crystalline silicon only, the critical forces suddenly drop (Fig. 4). This phenomenon is observed for the three crystal orientations but at different pressure thresholds. This suggests that above a certain value of the applied pressure, the compressed lattice will facilitate the lithium atom diffusion. As this effect is absent in amorphous structures, it is related to the crystalline nature of the silicon. This drop of the critical force is an indication of a change in the diffusion regime.

By comparing the Li trajectories below and above the pressure at which the critical force drops, it can be seen: (i) below the threshold, Li atoms move by hopping from one site to the others. Even though there are several possibilities for the hopping sites, the diffusion is oriented towards the z-direction as a force is applied; (ii) above the threshold pressure, the direction of diffusion follows one specific crystallographic plane in a ballistic manner, accelerating the Li atom diffusion. The inclination of these planes with respect to the diffusion direction is different for the three crystal orientations. For instance, for the crystal oriented along ⟨100⟩, the lithium diffuses in the ⟨101⟩ direction i.e., with an angle of 45 degrees with respect to the surface. In the case of the crystal orientation ⟨111⟩, the ballistic-like diffusion is oriented along the ⟨113⟩ direction at 19 GPa.

This change in the diffusion regime illustrates the coupling between the stress and the lithiation. It also indicates that the orientation ⟨110⟩ is particularly interesting as it shows the lowest value of the threshold value of pressure. Therefore, stress engineering could modify the charging speed of the anode.

4. Effect of lithiation on local stresses and structure

In this section, we investigate the effect of lithiation on the stress field of silicon i.e., the reverse effect of that studied in the previous section.

4.1. Global lithiation process

The lithiation process is simulated by diffusing successive lithium atoms into a silicon structure with a ⟨100⟩ orientation. The same simulation box as in Section 3 (silicon crystal with vacuum above and below) is used, with a confining pressure of 1 GPa. Each 100 ps, a

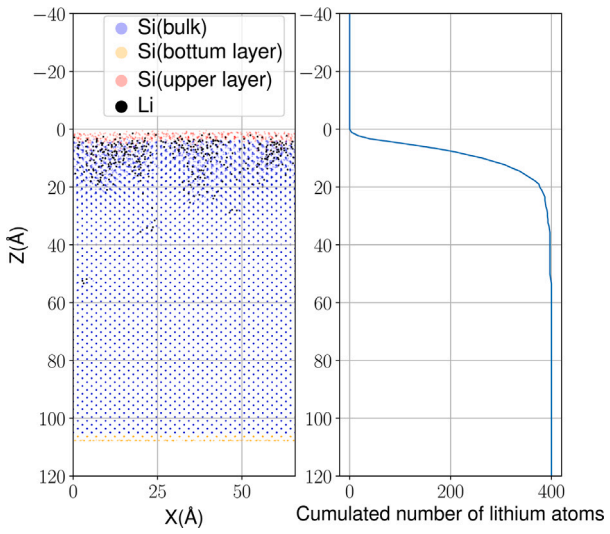

Fig. 5. (a) Lithium distribution obtained after insertion of 400 lithium atoms and (b) cumulative number of lithium atoms along z coordinate.

lithium atom is introduced in the vacuum area, under a field force equal to half the critical penetration force. This frequency is equivalent to a flux of 2.5×10^{-25} atom cm^{-2} s^{-1}. The initial position of lithium atoms is chosen randomly, both in z direction (between 210 Å and 200 Å from the vacuum box upper limit above silicon) and in the x–y plane. A threshold of 2.71 Å (half the lattice size) was set for the minimum distance between lithium atoms, to insure numerical simulation stability. Once a chosen number of lithium atoms has been inserted, equilibration step of 120 ps is applied.

4.2. Lithium diffusion inside silicon

The lithium atom distribution obtained after insertion of 400 lithium atoms is illustrated in Fig. 5(a), while the cumulative number of lithium atoms versus z coordinate is plotted in Fig. 5(b).

Firstly, the number of lithium atoms increases linearly with depth until approximately 15 Å depth, which corresponds to a layer of homogeneous lithium concentration, defined as "lithiated layer" here. The thickness of the lithiated layer is determined by the intersection of a linear approximation slope with the vertical axis corresponding to the total number of lithium atoms (17 Å in Fig. 5(a)). In addition, some lithium atoms are not trapped inside the lithiated layer, and diffuse through the silicon structure, even though the force applied is smaller than the critical force calculated in Section 3. As observed in Fig. 5(a), between 17 Å and 45 Å in depth, the concentration of lithium atoms is very low and is highly inhomogeneous. However, this phenomenon is marginal (few atoms) and occurs only when lithium atoms are by pairs or triplet.

In a second step, we increased the number of lithium atoms inserted into the silicon structure. The ratio between the total number of lithium atoms in the whole structure and the number of silicon atoms contained in the lithiated layer is calculated to give the lithium density. This density is compared to the thickness of this lithiated layer in Fig. 6 for various quantity of inserted lithium atoms. Both the density and thickness of this layer increase as the quantity of lithium atoms increases. It means that the diffusion length of lithium atoms is mainly restricted to the lithiated layer with an increasing lithium atom concentration. The thickness of the lithiated layer increases slowly enough and could be interpreted as the "lithiation front" and its thickness and sharpness are of the same range as those observed experimentally (Liu et al., 2012; McDowell et al., 2013).

Besides, for computational time reasons, our simulations apply a much higher lithium flux rate than the experimental values reported in the literature. This several order of magnitude difference could question the relevance of Molecular Dynamics simulations. However, we performed as well numerical simulations at two to four times lower fluxes, and the results were unchanged in terms of lithiated layer thickness and lithium concentration.

4.3. Stress field in the lithiated silicon

The stress tensor is calculated as in Section 2 by averaging the calculated stresses over the last 100 ps of the equilibration step. Afterwards, the difference between the final stresses and the residual stresses is calculated. Only the nodes that belong to the elements of the grid containing a lithium atom are taken into account.

The variation of hydrostatic and von Mises stresses is studied after the diffusion of 50, 100, 400 and 1000 lithium atoms compared to the non-lithiated configuration. Fig. 7 represents the evolution of the averaged pressure and von Mises components calculated from the stress variation tensor as a function of the lithium density for two temperatures 10 K and 300 K.

Globally, the amplitude of the averaged stresses due to lithiation tends to increase with the lithium density. This effect is even more marked at 300 K than at 10 K. In all cases, the increase of pressure is more important than that of von Mises (shear) stress: the hydrostatic stress is about five times higher than the von Mises stress. This means that lithiation induced a combination of compressive and shear stresses, thus giving rise to possible crack initiation and propagation, as incidentally observed experimentally (Shi et al., 2016). Note that the calculated compressive stresses are of the same order as that observed by optical sensor techniques (Sethuraman et al., 2010) . This effect is one of the issues in using silicon as anode for LIBs. The cracks in bulk silicon generate an increase of the solid-electrolyte interphase (SEI), a sink for Li atoms leading to the capacity fading of the battery. Preventing this effect in the future would be crucial for the durability of LIBs.

It is remarkable that the measured internal stress values may overpass three or four times the externally applied stress (1 GPa). This is due to the additional force exerted on the lithium ions to ensure their penetration in the bulk. Moreover, the averaged internal stress increase is not linear as a function of the lithium density (doubling lithium atom numbers does not lead to a doubling of stresses) (Fig. 7). This could be explained by the fact that the lithiated layer thickness increases, preventing stress concentration. For the largest number of lithium atoms, at 10 K, stress components tend to saturate, while at room temperature, the hydrostatic stress component still increases strongly, suggesting that the durability of LIBs could also be augmented with temperature control.

Fig. 8 shows the distribution of the hydrostatic and von Mises stresses in the lithiated layer for different density of lithium. The calculations have been performed at two temperatures (10 K and 300 K) for the orientation ⟨100⟩ and at 10 K for the orientation ⟨111⟩. First, it can be seen that the density of lithium plays a major role on the distribution of hydrostatic stress with an increase of the distribution with the density. This broadening is more marked at 300 K with a mixture of compressive and tensile stresses. A similar effect is observed on the von Mises stress with a drastic increase of the mean value with the density of lithium (This value is eight times larger for a density of 80% compared to a density of 20% at 300 K for the orientation ⟨100⟩). The comparison between both orientations shows some differences. The hydrostatic stress distribution is narrower for ⟨111⟩ at 10 K while it is broader for the von Mises stress.

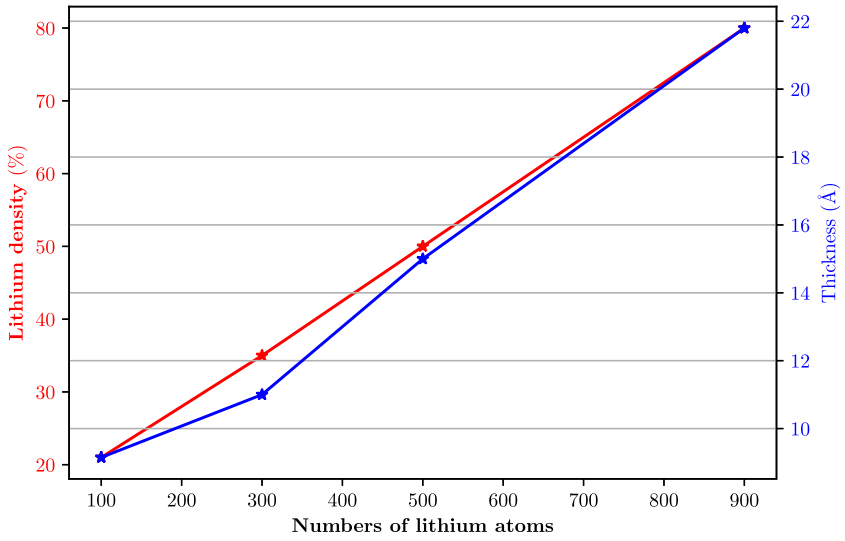

Fig. 6. Density and thickness of the lithiated layer for various numbers of lithium atoms at 10 K.

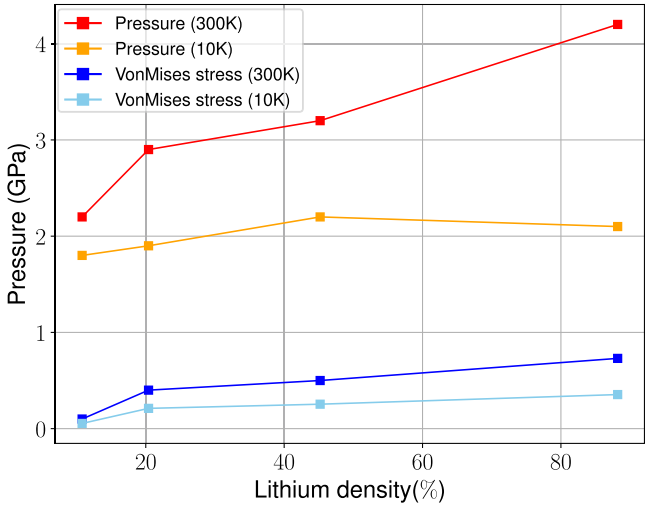

Fig. 7. Averaged pressure and von Mises additional stress versus the relative number of lithium atoms to the total number of atoms in the lithiated layer, at two temperatures 10 K and 300 K (variation with respect to non-lithiated configuration).

4.4. Evolution of local elastic moduli during lithiation

The variation of local elastic moduli with lithiation rate can be evaluated by imposing displacements on the upper layer of silicon atoms while clamping the bottom layer, or by moving the lateral boundaries of the box in order to apply a global strain on the system. The numerical simulations are carried out in four steps. First, three initial structures are obtained at a temperature of 10 K, with lithiation rates corresponding to 20%, 50% and 80%, respectively (lithiation simulation). Second, each structure is equilibrated under an NVT ensemble for 120 ps. The coarse-grained stress tensors are calculated as in Section 2 with $\mathbf{r}$ located on the nodes a regular grid with a regular spacing of 5 Å between the nodes. The calculated stress components are averaged over the last 100 s of the equilibration step. Third, six loading cases corresponding to global strain components $\epsilon_i = 10^{-4}$ with $i \in \{xx, yy, zz, xy, xz, yz\}$, are applied separately and one-by-one to the samples. Finally, each deformed configuration is equilibrated under NVT ensemble during 120 ps. For each loading case, the final stress tensor is computed on each node of the grid, as the average of the stresses calculated over the last 100 s of the equilibration step. In a similar way the coarse-grained strain tensors with the same coarse-graining width $R = 8$ Å are obtained for the same time and on the same grid using the following expression allowing the preservation of the mass conservation equation at all scales (Goldhirsch and Goldenberg, 2005):

$$\epsilon_{\alpha\beta}(\mathbf{r},t) = \frac{1}{2\rho^2(\mathbf{r},t)} \sum_{ij} m_i m_j \phi\left(\mathbf{r}-\mathbf{r_j}\right) \left[\left(u_{ij\alpha}(t)\frac{\partial}{\partial r_\beta} + u_{ij\beta}(t)\frac{\partial}{\partial r_\alpha}\right)\right] \times \phi\left(\mathbf{r}-\mathbf{r_i}\right)$$

with $u_{ij\alpha}$ the relative displacement of atoms i and j in the direction α, and

$$\rho(\mathbf{r},t) = \sum_i m_i \phi\left(\mathbf{r}-\mathbf{r_i}\right)$$

the local coarse-grained mass density. This procedure is replicated for all three lithiation rates. This allows getting $6\times6 = 36$ linear equations for 21 unknown elastic moduli relating the local stress components to the local strain components. The local elastic moduli are calculated on each point of the grid in a similar way to the global elasticity moduli, by relating the local GC stress tensors for the six different loadings with the related local GC strain tensors. Only nodes belonging to grid elements containing a lithium atom are considered. Fig. 9 shows the resulting distribution of the elastic moduli and the Poisson ratio for the three lithium rates at a temperature of 10 K, assuming isotropic elasticity as indicated in the Appendix. Table 3 shows the average values of the moduli and the Poisson ratio. The results show clearly a softening of the mechanical properties with increasing lithiation rate.

4.5. Structural evolution

Finally, to study the effect of lithiation on the silicon structure, we computed the radial distribution function between the pairs of silicon atoms in the lithiated and non-lithiated region (Kirkwood and Boggs, 1942). The radial distribution function between two types of atoms a and b is defined as :

$$g_{ab}(\mathbf{r}) = (N_a N_b)^{-1} \sum_{i=1}^{N_a}\sum_{j=1}^{N_b} \langle\delta(|\mathbf{r_i}-\mathbf{r_j}|-\mathbf{r})\rangle \tag{6}$$

The average of g function is calculated over the last 100 instants of the equilibration phase spaced by time steps of 10 fs (LAMMPS procedure). The averaged $g(Si-Si)$ in the initial configuration and in the lithiated layer after insertion of 1000 lithium atoms, at a temperature

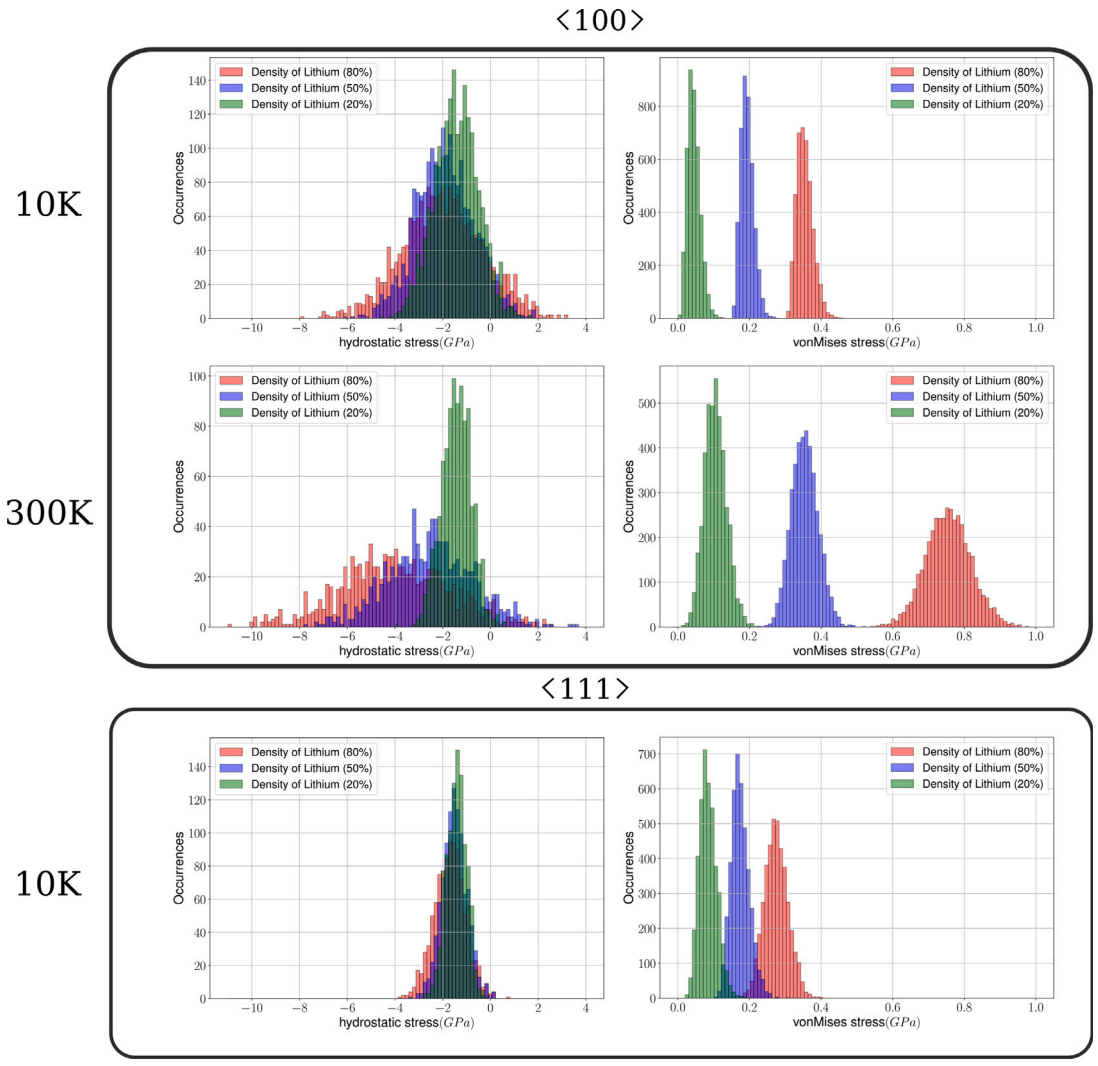

Fig. 8. Distribution of hydrostatic and von Mises additional stress for various lithium density for the orientation ⟨100⟩ at 10 K and 300 K, and for the orientation ⟨111⟩ at 10 K.

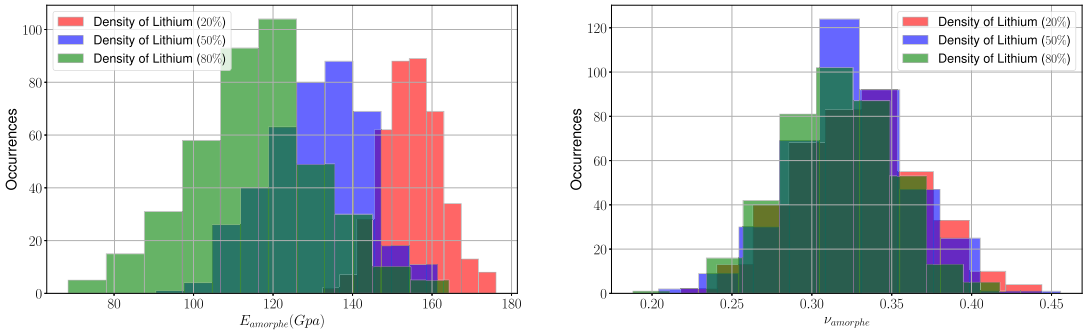

Fig. 9. Distribution of the elastic moduli and the Poisson ratio for the three lithium density, at a temperature of 10 K.

Table 3
Averaged and standard deviation of the elastic moduli and the Poisson ratio for the three lithium density, at a temperature of 10 K.

	$E_{amorphe}(GPa)$			$\nu_{amorphe}$		
	20%	50%	80%	20%	50%	80%
Average	154.76	131.24	115.41	0.325	0.323	0.315
Standard deviation	7.5	12.4	16.2	–	–	–

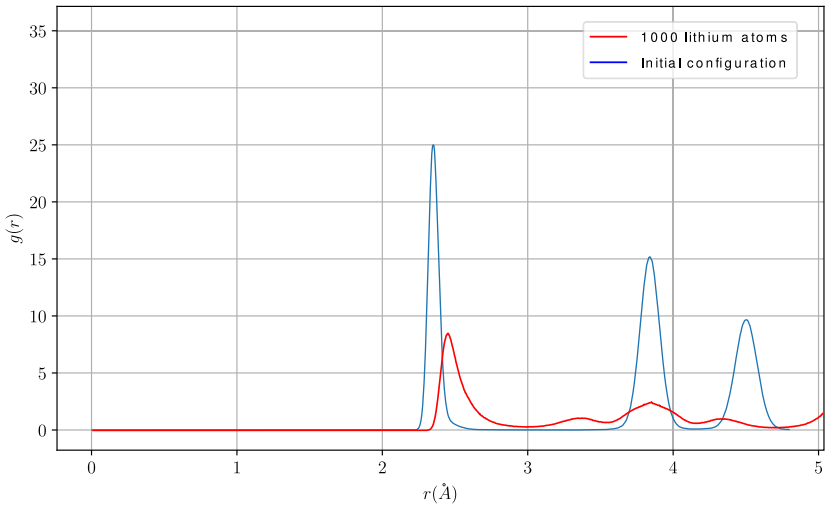

Fig. 10. Averaged $g(Si-Si)$ in the initial configuration and the lithiated layer after insertion of 1000 lithium atoms, at a temperature of 10 K.

of 10 K and for the orientation ⟨100⟩, are shown in Fig. 10. It clearly shows a progressive amorphization of the structure upon lithiation. For instance, the smaller shoulder at r= 3.35Åcorresponds to the appearance of fivefold coordinated defects observed in simulated amorphous silicon (Fusco et al., 2010). This effect corresponds to the experimental observations of the amorphization of silicon during lithiation (Liu et al., 2012). This solid-state amorphization is usually attributed to a chemical effect associated to the transition from the underlying crystalline structure with fixed composition, to a metastable amorphous alloy (Limthongkul et al., 2003). However, our work opens the possibility of a complementary hypothesis associated to the generated mechanical stresses: a pressure-induced amorphization and more generally stress-induced amorphization phenomenon could be as well at the origin of the crystal-to-amorphous transformation during the lithiation (Machon et al., 2014; Idrissi et al., 2022). For instance, amorphization of silicon has already been observed under indentation (Clarke et al., 1988).

Therefore, these results clearly illustrate that the hydrostatic and shear stresses are strongly dependent on the density of lithium, the temperature and on the crystalline orientation of the free surface. The simulations show that the lithiation induced a complex local stress field that influences the structural and probably physical and chemical properties of the sample.

5. Conclusions

To conclude, these results bring some insight to help the fundamental understanding of the mechanical effects induced by the lithiation of silicon occurring during lithium batteries charging. We showed how the mechanical and (electro)chemical mechanisms influenced each others, in particular the effect of stress on the diffusion regime of lithium in silicon, and the local stresses generated in silicon structures during lithiation, at different temperatures.

The critical penetration force, i.e., the minimum force necessary to avoid trapping of the lithium atom inside the silicon structure has been evaluated at various confining pressures. These latter were found to globally increase the value of this critical force for all silicon structures (crystalline and amorphous). However, above a certain confining pressure value, the force is observed to drop. This may be explained by the fact that lithium diffusion is eased when diffusing along preferential crystallographic planes. This result shows the drastic effect of mechanical conditions on the lithiation, a (electro)chemical process. This is a major finding as this opens potentially a way to modify the lithiation process through strain engineering. In addition, the fact that the value of the threshold pressure is not similar for all orientations gives a possibility of choice to activate or not the different diffusion regimes. This result must trigger some experimental works to confirm our results based on simulations.

Secondly, the reverse effect, i.e., how the lithiation generates mechanical stresses, in particular local stresses, is studied. Simulations indicates that lithiation occurs through a sharp lithiation front in agreement with experimental observations.

Determination of the stress field in the lithiated layer shows that the averaged stress increases as the concentration of lithium atom increases. The distribution of all stresses are inhomogeneous and the level of stresses (hydrostatic or von Mises) reaches values that may be critical for the silicon integrity. This effect is however smaller at very low temperature. This clearly illustrates that the hydrostatic and shear stresses are strongly dependent on the density of lithium, on the temperature and on the crystalline orientations of the silicon. The simulations show that the lithiation induced a complex local stress field that influences the structural and probably physical and chemical properties.

The analysis of the sensitivity of local stress to lithium shows a marked effect on the hydrostatic component, thus suggesting the use of pressure absorbing structures (like porous materials, or auxetic structures) to prevent the occurrence of excessive mechanical strains that induce damage. This effect is however less marked at very low temperature than at ambient temperature. A deeper understanding of optimized structures has now to be done at large scales, using the appropriate constitutive laws that have been identified at the local scale.

Declaration of competing interest

The authors declare that they have no known competing financial interests or personal relationships that could have appeared to influence the work reported in this paper.

Data availability

Data will be made available on request.

Acknowledgements

This work was supported by funding from the French National Centre for Scientific Research (CNRS) under the 80 Prime program and the French Ministry of Higher Education and Research (MEDRI).

Appendix

To compute the best fit of the general compliance matrix M_{ij} to the isotropic matrix C_{ij} we have defined an error function :

$$f(\underbrace{\frac{1}{E}}_{x},\underbrace{\frac{\nu}{E}}_{y}) = \sum_i \sum_j (M_{ij} - C_{ij})^2 \tag{7}$$

with

$$\underline{C} = \begin{bmatrix} x & -y & -y & 0 & 0 & 0 \\ -y & x & -y & 0 & 0 & 0 \\ -y & -y & x & 0 & 0 & 0 \\ 0 & 0 & 0 & x+y & 0 & 0 \\ 0 & 0 & 0 & 0 & x+y & 0 \\ 0 & 0 & 0 & 0 & 0 & x+y \end{bmatrix} \tag{8}$$

The best approximation corresponds to the solution of the following system :

$$\begin{cases} \frac{\partial f}{\partial x} = 0 \\ \frac{\partial f}{\partial y} = 0 \end{cases} \tag{9}$$

This gives the following :

$$\begin{cases} 6 \times x + 3 \times y = M_{11} + M_{22} + M_{33} + M_{44} + M_{55} + M_{66} \\ 9 \times y + 3 \times x = M_{44} + M_{55} + M_{66} - 2 \times M_{12} - 2 \times M_{13} - 2 \times M_{23} \end{cases} \tag{10}$$

The solution of this system (x_0, y_0) leads to the isotropic modulus:

$$\begin{cases} E = \frac{1}{x_0} \\ \nu = \frac{y_0}{x_0} \end{cases} \tag{11}$$

The error of this approximation corresponds to :

$$Erreur = \frac{f(x_0, y_0)}{\sum_i \sum_j (C_{ij}(x_0, y_0))^2} \tag{12}$$

where $C_{ij}(x_0, y_0)$ are the coefficients of the compliance matrix corresponding to the solution (x_0, y_0).

References

Armand, M., Axmann, P., Bresser, D., Copley, M., Edström, K., Ekberg, C., Guyomard, D., Lestriez, B., Novák, P., Petranikova, M., Porcher, W., Trabesinger, S., Wohlfahrt-Mehrens, M., Zhang, H., 2020. Lithium-ion batteries – Current state of the art and anticipated developments. J. Power Sources 479, 228708. http://dx.doi.org/10.1016/j.jpowsour.2020.228708, URL http://www.sciencedirect.com/science/article/pii/S0378775320310120.

Bagheri, A., Arghavani, J., Naghdabadi, R., 2019. On the effects of hydrostatic stress on Li diffusion kinetics and stresses in spherical active particles of Li-ion battery electrodes. Mech. Mater. 137, 103134, Publisher: Elsevier.

Bagheri, A., Arghavani, J., Naghdabadi, R., Brassart, L., 2021. A theory for coupled lithium insertion and viscoplastic flow in amorphous anode materials for Li-ion batteries. Mech. Mater. 152, 103663, Publisher: Elsevier.

Baskes, M.I., 1992. Modified embedded-atom potentials for cubic materials and impurities. Phys. Rev. B 46 (5), 2727–2742. http://dx.doi.org/10.1103/PhysRevB.46.2727, URL https://link.aps.org/doi/10.1103/PhysRevB.46.2727.

Berckmans, G., De Sutter, L., Marinaro, M., Smekens, J., Jaguemont, J., Wohlfahrt-Mehrens, M., van Mierlo, J., Omar, N., 2019. Analysis of the effect of applying external mechanical pressure on next generation silicon alloy lithium-ion cells. Electrochim. Acta 306, 387–395. http://dx.doi.org/10.1016/j.electacta.2019.03.138, URL https://www.sciencedirect.com/science/article/pii/S0013468619305614.

Clarke, D.R., Kroll, M.C., Kirchner, P.D., Cook, R.F., Hockey, B.J., 1988. Amorphization and Conductivity of Silicon and Germanium Induced by Indentation. Phys. Rev. Lett. 60 (21), 2156–2159. http://dx.doi.org/10.1103/PhysRevLett.60.2156, URL https://link.aps.org/doi/10.1103/PhysRevLett.60.2156.

Francis, J.G.F., 1961. The QR Transformation a Unitary Analogue to the LR Transformation—Part 1. Comput. J. 4 (3), 265–271. http://dx.doi.org/10.1093/comjnl/4.3.265, URL https://doi.org/10.1093/comjnl/4.3.265.

Francis, J.G.F., 1962. The QR Transformation—Part 2. Comput. J. 4 (4), 332–345. http://dx.doi.org/10.1093/comjnl/4.4.332.

Fusco, C., Albaret, T., Tanguy, A., 2010. Role of local order in the small-scale plasticity of model amorphous materials. Phys. Rev. E 82 (6), 066116. http://dx.doi.org/10.1103/PhysRevE.82.066116, URL https://link.aps.org/doi/10.1103/PhysRevE.82.066116.

Goldhirsch, I., Goldenberg, C., 2002. On the microscopic foundations of elasticity. Eur. Phys. J. E 9 (3), 245–251. http://dx.doi.org/10.1140/epje/i2002-10073-5, URL http://dx.doi.org/10.1140/epje/i2002-10073-5.

Goldhirsch, I., Goldenberg, C., 2005. Continuum mechanics for small systems and fine resolutions. In: HandbOok of Theoretical and Computational Nanotechnology. pp. 1–58.

Hall, J.J., 1967. Electronic effects in the elastic constants of n-type silicon. Phys. Rev. 161 (3), 756.

Huang, P., Guo, Z., 2021. Li-ion distribution and diffusion-induced stress calculations of particles using an image-based finite element method. Mech. Mater. 157, 103843, Publisher: Elsevier.

Idrissi, H., Carrez, P., Cordier, P., 2022. On amorphization as a deformation mechanism under high stresses. Curr. Opin. Solid State Mater. Sci. 26 (1), 100976. http://dx.doi.org/10.1016/j.cossms.2021.100976, URL https://www.sciencedirect.com/science/article/pii/S1359028621000796.

Kirkwood, J.G., Boggs, E.M., 1942. The Radial Distribution Function in Liquids. J. Chem. Phys. 10 (6), 394–402. http://dx.doi.org/10.1063/1.1723737, URL https://aip.scitation.org/doi/abs/10.1063/1.1723737.

Kublanovskaya, V.N., 1962. On some algorithms for the solution of the complete eigenvalue problem. USSR Comput. Math. Math. Phys. 1 (3), 637–657. http://dx.doi.org/10.1016/0041-5553(63)90168-X, URL https://www.sciencedirect.com/science/article/pii/004155536390168X.

Kumta, P.N., Hepp, A., Datta, M., Velikokhatnyi, O.I., 2021. Silicon Anode Systems for Lithium-Ion Batteries. Elsevier, Google-Books-ID.

Limthongkul, P., Jang, Y.-I., Dudney, N.J., Chiang, Y.-M., 2003. Electrochemically-driven solid-state amorphization in lithium–metal anodes. J. Power Sources 119–121, 604–609. http://dx.doi.org/10.1016/S0378-7753(03)00303-3, URL https://www.sciencedirect.com/science/article/pii/S0378775303003033.

Liu, X.H., Wang, J.W., Huang, S., Fan, F., Huang, X., Liu, Y., Krylyuk, S., Yoo, J., Dayeh, S.A., Davydov, A.V., Mao, S.X., Picraux, S.T., Zhang, S., Li, J., Zhu, T., Huang, J.Y., 2012. In situ atomic-scale imaging of electrochemical lithiation in silicon. Nature Nanotechnol. 7 (11), 749–756. http://dx.doi.org/10.1038/nnano.2012.170, URL https://www.nature.com/articles/nnano.2012.170.

Lu, Y., Ni, Y., 2015. Effects of particle shape and concurrent plasticity on stress generation during lithiation in particulate Li-ion battery electrodes. Mech. Mater. 91, 372–381, Publisher: Elsevier.

Machon, D., Meersman, F., Wilding, M.C., Wilson, M., McMillan, P.F., 2014. Pressure-induced amorphization and polyamorphism: Inorganic and biochemical systems. Prog. Mater. Sci. 61, 216–282. http://dx.doi.org/10.1016/j.pmatsci.2013.12.002, URL https://www.sciencedirect.com/science/article/pii/S007964251300087X.

McBrayer, J.D., Apblett, C.A., Harrison, K.L., Fenton, K.R., Minteer, S.D., 2021. Mechanical studies of the solid electrolyte interphase on anodes in lithium and lithium ion batteries. Nanotechnology 32 (50), 502005. http://dx.doi.org/10.1088/1361-6528/ac17fe, URL https://doi.org/10.1088/1361-6528/ac17fe.

McDowell, M.T., Lee, S.W., Nix, W.D., Cui, Y., 2013. 25Th Anniversary Article: Understanding the Lithiation of Silicon and Other Alloying Anodes for Lithium-Ion Batteries. Adv. Mater. 25 (36), 4966–4985. http://dx.doi.org/10.1002/adma.201301795, URL https://onlinelibrary.wiley.com/doi/abs/10.1002/adma.201301795.

McDowell, M.T., Ryu, I., Lee, S.W., Wang, C., Nix, W.D., Cui, Y., 2012. Studying the Kinetics of Crystalline Silicon Nanoparticle Lithiation with In Situ Transmission Electron Microscopy. Adv. Mater. 24 (45), 6034–6041. http://dx.doi.org/10.1002/adma.201202744, URL https://onlinelibrary.wiley.com/doi/abs/10.1002/adma.201202744.

McDowell, M.T., Xia, S., Zhu, T., 2016. The mechanics of large-volume-change transformations in high-capacity battery materials. Extreme Mech. Lett. 9, 480–494. http://dx.doi.org/10.1016/j.eml.2016.03.004, URL https://www.sciencedirect.com/science/article/pii/S2352431616300037.

McSkimin, H.J., 1953. Measurement of Elastic Constants at Low Temperatures by Means of Ultrasonic Waves–Data for Silicon and Germanium Single Crystals, and for Fused Silica. J. Appl. Phys. 24 (8), 988–997. http://dx.doi.org/10.1063/1.1721449, URL https://aip.scitation.org/doi/10.1063/1.1721449.

Middelmann, T., Walkov, A., Bartl, G., Schödel, R., 2015. Thermal expansion coefficient of single-crystal silicon from 7 K to 293 K. Phys. Rev. B 92 (17), 174113. http://dx.doi.org/10.1103/PhysRevB.92.174113, URL https://link.aps.org/doi/10.1103/PhysRevB.92.174113.

Molnár, G., Ganster, P., Török, J., Tanguy, A., 2016. Sodium effect on static mechanical behavior of MD-modeled sodium silicate glasses. J. Non-Crystal. Solids 440, 12–25.

Obrovac, M.N., Chevrier, V.L., 2014. Alloy negative electrodes for Li-ion batteries. Chem. Rev. 114 (23), 11444–11502.

Obrovac, M.N., Christensen, L., 2004. Structural Changes in Silicon Anodes during Lithium Insertion/Extraction. Electrochemical and Solid-State Letters 7 (5), A93. http://dx.doi.org/10.1149/1.1652421, https://iopscience.iop.org/article/10.1149/1.1652421/meta, Publisher: IOP Publishing.

Pan, J., Zhang, Q., Li, J., Beck, M.J., Xiao, X., Cheng, Y.-T., 2015. Effects of stress on lithium transport in amorphous silicon electrodes for lithium-ion batteries. Nano Energy 13, 192–199. http://dx.doi.org/10.1016/j.nanoen.2015.02.020, URL https://www.sciencedirect.com/science/article/pii/S2211285515000798.

Sethuraman, V.A., Chon, M.J., Shimshak, M., Srinivasan, V., Guduru, P.R., 2010. In situ measurements of stress evolution in silicon thin films during electrochemical lithiation and delithiation. J. Power Sources 195 (15), 5062–5066. http://dx.doi.org/10.1016/j.jpowsour.2010.02.013, URL https://www.sciencedirect.com/science/article/pii/S0378775310002582.

Shang, S., Lu, Y., Yu, Z., Wang, J., Wang, F., 2021. Concurrent diffusion and creep in lithium-ion batteries. Mech. Mater. 155, 103731, Publisher: Elsevier.

Shi, F., Song, Z., Ross, P.N., Somorjai, G.A., Ritchie, R.O., Komvopoulos, K., 2016. Failure mechanisms of single-crystal silicon electrodes in lithium-ion batteries. Nature Commun. 7 (1), 1–8.

Thompson, A.P., Aktulga, H.M., Berger, R., Bolintineanu, D.S., Brown, W.M., Crozier, P.S., in 't Veld, P.J., Kohlmeyer, A., Moore, S.G., Nguyen, T.D., Shan, R., Stevens, M.J., Tranchida, J., Trott, C., Plimpton, S.J., 2022. LAMMPS - a flexible simulation tool for particle-based materials modeling at the atomic, meso, and continuum scales. Computer Physics Communications 271, 108171. http://dx.doi.org/10.1016/j.cpc.2021.108171, https://www.sciencedirect.com/science/article/pii/S0010465521002836.

Tsamados, M., Tanguy, A., Goldenberg, C., Barrat, J.-L., 2009. Local elasticity map and plasticity in a model Lennard-Jones glass. Phys. Rev. E 80 (2), 026112.

Tunuguntla, D.R., Thornton, A.R., Weinhart, T., 2016. From discrete elements to continuum fields: Extension to bidisperse systems. Comput. Part. Mech. 3 (3), 349–365. http://dx.doi.org/10.1007/s40571-015-0087-y, URL http://arxiv.org/abs/1504.00202.

Wang, H., Ji, X., Chen, C., Xu, K., Miao, L., 2013. Lithium diffusion in silicon and induced structure disorder: A molecular dynamics study. AIP Adv. 3 (11), 112102. http://dx.doi.org/10.1063/1.4829440, URL https://aip.scitation.org/doi/10.1063/1.4829440.

Wu, H., Cui, Y., 2012. Designing nanostructured Si anodes for high energy lithium ion batteries. Nano Today 7 (5), 414–429. http://dx.doi.org/10.1016/j.nantod.2012.08.004, URL http://www.sciencedirect.com/science/article/pii/S1748013212000977.

Yan, X., Gouissem, A., Sharma, P., 2015. Atomistic insights into Li-ion diffusion in amorphous silicon. Mech. Mater. 91, 306–312. http://dx.doi.org/10.1016/j.mechmat.2015.04.001, URL https://www.sciencedirect.com/science/article/pii/S0167663615000836.

Yang, H., Liang, W., Guo, X., Wang, C.-M., Zhang, S., 2015. Strong kinetics-stress coupling in lithiation of Si and Ge anodes. Extreme Mech. Lett. 2, 1–6. http://dx.doi.org/10.1016/j.eml.2014.11.008, URL https://www.sciencedirect.com/science/article/pii/S235243161400011X.

Zhang, F., Huang, Q.-A., Tang, Z., Li, A., Shao, Q., Zhang, L., Li, X., Zhang, J., 2020. A review of mechanics-related material damages in all-solid-state batteries: Mechanisms, performance impacts and mitigation strategies. Nano Energy 70, 104545.

Zhao, K., Cui, Y., 2016. Understanding the role of mechanics in energy materials: A perspective. Extreme Mech. Lett. 9, 347–352. http://dx.doi.org/10.1016/j.eml.2016.10.003, URL https://www.sciencedirect.com/science/article/pii/S2352431616302152.

Zimmerman, J.A., WebbIII, E.B., Hoyt, J.J., Jones, R.E., Klein, P.A., Bammann, D.J., 2004. Calculation of stress in atomistic simulation. Modelling Simul. Mater. Sci. Eng. 12 (4), S319.